World Electric Vehicle Journal

MDPI

Article

Optimized Design of a Permanent Magnet Machine for Golf Carts Under Multiple Operating Conditions

Wenye Wu [1,2,*], Donghui Li [1] and Weifeng Wang [3]

[1] School of Electrical and Information Engineering, Tianjin University, Tianjin 300072, China; lidonghui@tju.edu.cn
[2] School of Automotive Engineering, Suzhou University of Technology, Suzhou 215500, China
[3] NBSL M&E Technology Co., Ltd., Shanghai 201611, China; wang.weifeng@nbsl.com
* Correspondence: 201900040@szut.edu.cn

Abstract

In response to the growing demand for efficient and eco-friendly golf carts, this paper presents an optimized design of a permanent magnet synchronous machine (PMSM) for multiple operating conditions. The application scenarios of the golf cart were first analyzed, identifying the power requirements under three driving conditions such as unloaded on flat roads, fully loaded on flat roads, and fully loaded on slopes. Then, a 36-slot 8-pole interior PMSM is developed, and a systematic two-stage optimization strategy using a Multi-Objective Genetic Algorithm (MOGA) is applied to enhance both no-load and rated-load performance. By adjusting key rotor parameters to balance competing objectives, the optimized machine demonstrates notable improvements in cogging torque reduction, output torque, torque ripple minimization, and operational efficiency. Specifically, the results show that the optimized machine achieves a cogging torque reduction of over 60%, an increase in maximum output torque by 7.3%, and a peak efficiency improvement of 1.2 percentage points under high-load conditions. Experimental results validate the effectiveness of the design and confirm its suitability for the complex operating conditions of golf carts.

Keywords: electric golf cart; optimization design; permanent magnet synchronous machine; multiple operating conditions

check for updates

Academic Editor: Vladimir Katic

Received: 19 October 2025
Revised: 12 December 2025
Accepted: 13 December 2025
Published: 18 December 2025

Citation: Wu, W.; Li, D.; Wang, W. Optimized Design of a Permanent Magnet Machine for Golf Carts Under Multiple Operating Conditions. *World Electr. Veh. J.* **2025**, *16*, 680. https://doi.org/10.3390/wevj16120680

Copyright: © 2025 by the authors. Published by MDPI on behalf of the World Electric Vehicle Association. Licensee MDPI, Basel, Switzerland. This article is an open access article distributed under the terms and conditions of the Creative Commons Attribution (CC BY) license (https://creativecommons.org/licenses/by/4.0/).

1. Introduction

With the continuous growth of the global economy and the improvement of material living standards, there is an increasing demand for spiritual and cultural enrichment. Lifestyles are gradually becoming more diversified, with life needs transitioning from a "subsistence-oriented" model to a "culture-oriented" one. Driven by the dissemination and popularity of golf culture, a growing number of people are heading to golf courses, thereby stimulating market demand [1–3]. As an essential electric transportation solution, the golf cart is a small vehicle specifically designed for use on golf courses, providing golfers and spectators with more convenient mobility and an enhanced viewing experience. In the current context of technological advancement and rising demand for green, low-carbon, and environmentally friendly solutions, electric golf carts have gained increased attention due to their inherent advantages, such as zero emissions, low noise, and energy efficiency. These characteristics align well with ideal expectations, making the application of electric golf carts in golf courses a focal point of interest in the field of golf sports [4,5].

The drive system serves as the core component of an electric golf cart, directly determining its dynamic performance, operational efficiency, and reliability. Golf carts typically need to navigate varied terrains, often characterized by complex operating conditions. These include high-speed travel on level ground, full-load climbing on slopes, and low-speed waiting periods. Such diverse scenarios impose stringent and multi-faceted demands on the drive machine, requiring high torque output at low speeds for hill climbing, high efficiency at medium speeds for cruising, and low torque ripple for smooth operation at low speeds. Particularly for cost-sensitive applications like light electric vehicles, reducing the use of expensive permanent magnet materials while maintaining high performance is a critical design objective [6]. However, the high-efficiency zones of conventional drive machines often fail to align optimally with the cart's frequently used operating points. This mismatch can lead to excessive energy consumption and reduced battery life, highlighting a critical challenge in the current design of drive systems for electric golf carts [7–10].

Permanent magnet synchronous machines (PMSMs), especially interior permanent magnet synchronous machines (IPMSMs), have gained increasing attention in such applications owing to their high power density, high efficiency, and extended constant power speed range. The built-in permanent magnet configuration of IPMSMs not only ensures high torque density via permanent magnet torque, but also contributes considerable reluctance torque. This feature makes them particularly well-suited for applications requiring high overload capability, such as slope climbing [11]. However, the design of an IPMSM that simultaneously satisfies the competing objectives of high torque output, low torque ripple, and high efficiency under multiple operating conditions remains a challenging endeavor. Critical design parameters—including electric and magnetic loadings, permanent magnet dimensions, and rotor geometry features such as magnetic bridges and flux barriers—require careful multi-objective optimization to achieve an effective balance among these performance criteria [12–14]. Notably, common torque-ripple mitigation techniques, such as fractional slot windings, stator/rotor skewing, or complex multi-barrier rotor designs, often introduce trade-offs in manufacturing complexity, cost, or torque density [15,16]. In contrast, the rotor surface notch method adopted in this work provides a structurally simpler and more manufacturing-friendly alternative, which is particularly advantageous for cost-sensitive applications like golf carts [15,16].

To address the aforementioned challenges, this paper focuses on the multi-condition optimization design of a high-efficiency permanent magnet machine specifically for golf carts. A 36-slot 8-pole IPMSM is developed based on the power requirements derived from vehicle dynamics. The optimization process is systematically conducted in two stages: a no-load optimization targeting flux linkage and cogging torque, followed by a rated-load optimization focusing on output torque, torque ripple, and efficiency. A MOGA is employed to navigate the design trade-offs [17,18]. While multi-objective optimization for general EV traction is well-established, the novelty of this work lies in its specific application to the unique multi-condition duty cycle of golf carts and the implementation of a systematic two-stage optimization strategy. This approach effectively decouples the conflicting design objectives for no-load and rated-load conditions, a critical need for this application which has received limited attention. The proposed methodology ensures a balanced performance enhancement across all key operational scenarios specific to golf carts.

2. Machine Application Scenarios and Power Calculation

2.1. Driving Conditions and Requirements for Golf Carts

As a specialized transportation vehicle designed for golf courses, the electric golf cart is a compact unit that must accommodate various operational scenarios such as rapid movement, full-load climbing, and low-speed waiting within the sports field. Since golf

courses are typically constructed in hilly terrain with moderate slopes, golf carts are required to perform under complex driving conditions [19]. For instance, to ensure quick mobility across the course, the cart must achieve high speeds on flat roads, during which the drive machine operates under high-speed and low-torque conditions. When the vehicle is fully loaded and needs to climb an inclined slope, the drive system must deliver maximum torque output, generally at reduced speeds. Correspondingly, when the cart operates at full capacity on level ground, the machine typically runs at medium speed and medium torque.

However, in the actual design of golf cart drive systems, the high-efficiency zone of the drive machine often does not coincide with the vehicle's frequently used operating range. As illustrated in Figure 1, machine efficiency remains relatively low in the high-frequency operating region of the cart. This mismatch between operational requirements and machine performance characteristics results in excessive battery energy consumption.

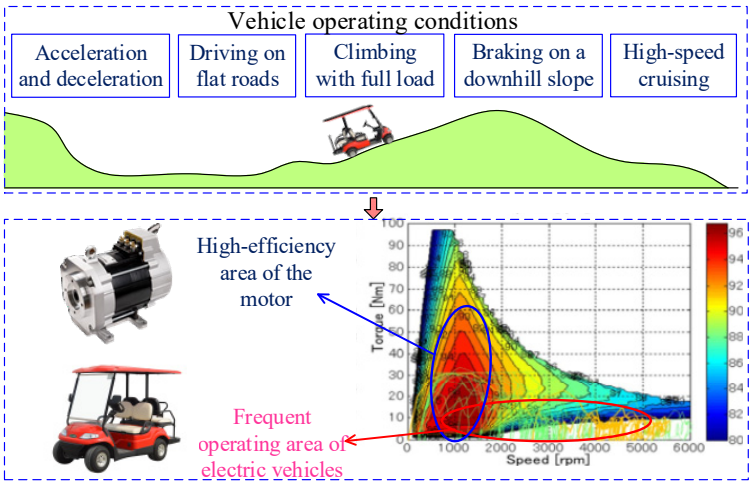


Figure 1. Operating conditions and drive requirements of golf carts.

2.2. Machine Power Calculation

This paper takes a small four-seat golf cart as the research object and develops a high-performance driving machine for it. Table 1 shows the parameters of the four-seater golf cart of the research object.

Table 1. Four-seater golf cart parameters.

Parameter Describe	Value	Parameter Describe	Value
Body dimensions (mm)	3075 × 1230 × 1895	Gradeability (%)	35 (19.3°)
Vehicle mass (kg)	458	Wheel radius (mm)	240
Full mass (kg)	758	Acceleration time (s)	15
Maximum speed (km/h)	35	Power cell voltage (V)	48
Transmission Ratio	16	Transmission Efficiency	0.9

In the design process of the IPMSM for the four-seater golf cart, the vehicle's power requirements are crucial for determining the machine parameters and performance. During operation, the golf cart receives electrical energy from the battery and delivers it to the machine. The machine then outputs mechanical power to overcome both the internal resistance of the mechanical system and the external resistance determined by the driving cycles. The maximum speed, acceleration time, and maximum gradability are selected as

performance evaluation criteria for vehicle dynamics. The equation of motion for the golf cart is established as follows [20]:

$$T_{tq} i \eta_T = r[mgf\cos\alpha + mg\sin\alpha + \frac{1}{2}\rho C_d A(u_a\frac{1000}{3600})^2 + \delta m\frac{du}{dt}] \quad (1)$$

In the equation, T_{tq} represents the drive machine torque, i denotes the final drive ratio, η_T indicates the transmission efficiency, r is the wheel radius, m is the vehicle mass, g stands for the gravitational force acting on the vehicle, f corresponds to the rolling resistance coefficient, α signifies the slope angle, ρ is the air density, C_d represents the air resistance coefficient, A denotes the frontal area of the vehicle, u_a indicates the vehicle speed, δ refers to the vehicle rotational mass conversion coefficient, and du/dt is the acceleration.

Based on the multi-condition operational requirements of the four-seater golf cart, three frequently encountered driving conditions—unloaded on flat road, fully loaded on flat road, and fully loaded on a slope—are selected to calculate the corresponding machine power, torque, and speed requirements. The power calculation is performed using the following power balance equation:

$$\begin{cases} P_{e1} = \frac{u_a}{3600\eta_T}\left[mgf\cos\alpha + \frac{1}{2}\rho C_d A(u_a\frac{1000}{3600})^2\right] \\ P_{e2} = \frac{u_a}{3600\eta_T}\left[(m+m_0)gf\cos\alpha + \frac{1}{2}\rho C_d A(u_a\frac{1000}{3600})^2\right] \\ P_{e3} = \frac{u_a}{3600\eta_T}\left[(m+m_0)gf\cos\alpha + \frac{1}{2}\rho C_d A(u_a\frac{1000}{3600})^2 + (m+m_0)g\sin\alpha\right] \end{cases} \quad (2)$$

Here, P_{e1}, P_{e2} and P_{e3} represent the power requirements under the unloaded flat road, fully loaded flat road, and fully loaded slope conditions, respectively, while m and m_0 denote the unloaded mass and fully loaded mass of the vehicle.

Based on the vehicle performance parameters of the four-seater golf cart, including requirements for maximum speed, acceleration time, and maximum gradability, the power demands for the unloaded flat road, fully loaded flat road, and fully loaded slope conditions were calculated using Equations (1) and (2). Key parameters critical to the vehicle dynamics calculation were selected as follows: a rolling resistance coefficient of 0.02, accounting for operation on turf and paved surfaces; an air resistance coefficient of 0.9, reflecting the vehicle's box-like profile; a target acceleration of 0.4 m/s^2, representing typical low-performance acceleration requirements; and a rotational mass conversion coefficient of 1.05, considering the simple single-stage reduction transmission system. For the fully loaded slope condition, the slope angle used in the calculation corresponds to the gradeability value provided in Table 1 (i.e., 19.3°). The calculation results are summarized in Table 2.

Table 2. Machine power requirements for the four-seater golf cart across different driving cycles.

Driving Cycles	Power (kW)	Speed (rpm)	Torque (Nm)
Unloaded on flat road	4.4	6192	6.7
Fully loaded on flat road	7.2	6324	10.9
Fully loaded on a slope	9.9	1807	52.4

3. Machine Configuration and Preliminary Design

3.1. Configuration and Characteristics

A 36-slot 8-pole IPMSM has been developed for golf cart propulsion systems, with its configuration illustrated in Figure 2. The stator incorporates specially designed slots with inclined shoulders and rounded bottoms to maintain a substantial yoke thickness, facilitating coil insertion and enhancing heat dissipation. A double-layer lap winding configuration is implemented in the stator. The rotor features a built-in V-shaped permanent magnet

arrangement that enables simultaneous production of both permanent magnet torque and reluctance torque, thereby providing enhanced torque output capability essential for hill-climbing requirements. To suppress torque ripple and back-EMF harmonics, symmetrically distributed notched slots are incorporated on the rotor surface under each pole.

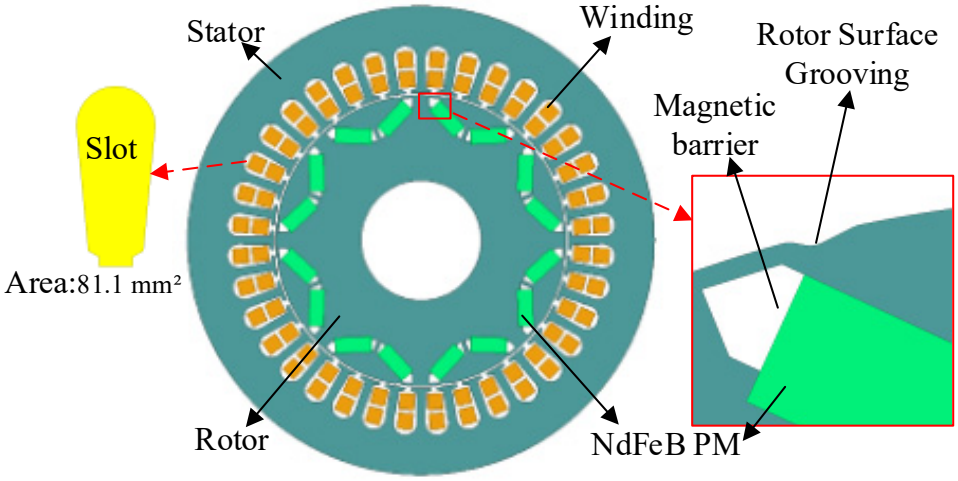


Figure 2. Machine configuration and specifics.

Based on the preceding analysis and calculation of the power requirements for the golf cart, the output parameters for the machine's rated operating conditions are determined. Given the vehicle's low-voltage (48 V) battery system, the winding design employs a lower number of turns to reduce the no-load back EMF. The specific machine parameters are summarized in Table 3.

Table 3. Main design specifications of the machine.

Parameters	Values	Parameters	Values
Rated power	5.5 kW	Stator outside diameter	155 mm
Rated speed	3000 rpm	Rotor outside diameter	98 mm
Maximum speed	7200 rpm	Stack length	100 mm
Rated torque	17.5 Nm	Air gap	0.8 mm
Number of turns	4	Winding type	Double-layer lap winding
PM property	N38UH	Insulation & Temperature Class	H (180 °C)
Slot Fill Factor	76%	Conductor details	5 × 0.9 mm + 2 × 0.8 mm

3.2. Selection and Design of Electric and Magnetic Loadings

The electric loading of a permanent magnet machine is constrained by the stator winding temperature rise and the demagnetization withstand capability of the rotor permanent magnets, whereas the magnetic loading is limited by the magnetic saturation level in the stator and rotor cores. There exists a fundamental trade-off between the electric and magnetic loadings in the machine. Figure 3 illustrates a simplified no-load magnetic flux path in a V-shaped IPMSM. As shown, the flux generated by the permanent magnets crosses the air gap and enters the stator teeth. When the magnetomotive force produced by the magnets remains constant, the magnetic flux density in the stator teeth is governed by the degree of magnetic saturation in the teeth.

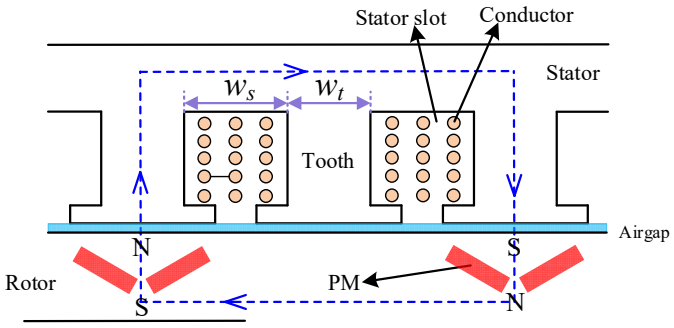


Figure 3. Simplified magnetic circuit model of an IPMSM under no-load conditions.

Assuming a constant stator slot height and sufficient flux-carrying capacity in the stator yoke, the stator slot width w_s and tooth width w_t exhibit a trade-off relationship in terms of their influence on magnetic and current density. A larger slot width w_s increases the slot area, enabling the use of thicker conductors for a given number of turns, which corresponds to a lower current density, as depicted in Figure 4. Conversely, a larger tooth width w_t allows more magnetic flux to pass through, leading to a reduction in magnetic flux density.

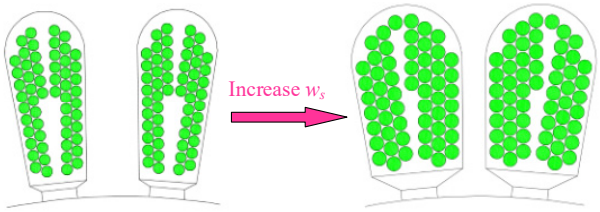


Figure 4. Variation in conductor cross-sectional area with increasing of slot width w_s.

Since the golf cart in this research needs to climb a 35% steep slope, the rotor permanent magnets of the machine are made of neodymium iron boron (NdFeB), a rare-earth permanent magnet material with high remanence and high coercivity. When the operating point of the permanent magnet is designed to be at the maximum energy product, the volume of the permanent magnet is minimized. Based on this condition, the thickness and cross-sectional area of the permanent magnet can be calculated using the following formulas:

$$h_m = \frac{2k_s k_\delta B_\delta \delta_g}{\mu_0 H_c} \tag{3}$$

$$S_{\mathrm{m}} = \frac{2k_s k_\delta B_\delta \delta_g}{B_r} \tag{4}$$

In the above formulas, k_s and k_δ denote the saturation coefficients of the stator/rotor iron cores and the air gap, respectively; δ_g represents the air gap length, and μ_0 corresponds to the relative permeability of the iron core. The magnetic flux density in the air gap is expressed as B_δ, whereas B_r and H_c indicate the remanent magnetic flux density and coercivity of the permanent magnet, respectively.

Based on the above analysis, the cross-sectional dimensions of the machine rotor permanent magnet are preliminarily set at 5.3 mm × 11.6 mm. On this basis, the magnetic flux density and current density of the machine are further determined. The magnetic flux density values are obtained by monitoring the magnetic field at the midpoint of the stator tooth, while the current density is adjusted by increasing or decreasing the conductor wire diameter under the condition of a constant number of conductors, thereby altering the current density value. Under the condition of maintaining constant stator yoke dimensions, varying the stator slot width allows adjustment of the conductor current density in the

slot and the magnetic flux density in the tooth. Figure 5 shows the variation trends of the conductor current density (J) and tooth magnetic flux density (B) as the stator slot width w_s increases from 3.0 mm to 6.0 mm. Here, B_0, B_1, and B_2 represent the tooth magnetic flux density under no-load, rated load, and maximum load conditions, respectively, while J_1 and J_2 denote the current density under rated load and maximum load conditions.

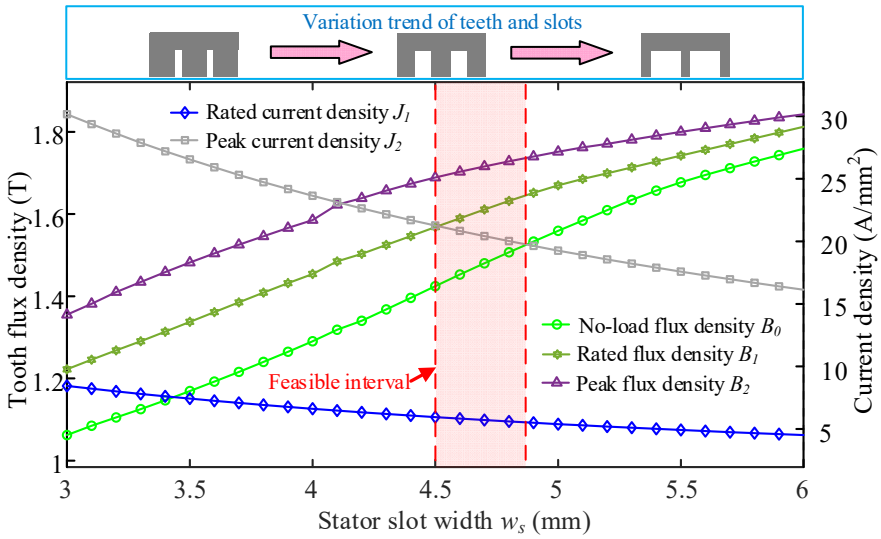


Figure 5. Variation in machine current density and magnetic flux density with stator tooth/slot width.

It can be observed that as the stator slot width w_s increases, the conductor current density decreases. Under maximum load conditions, the current density drops from 30.2 A/mm^2 to 16.1 A/mm^2. In contrast, the magnetic flux density in the tooth exhibits an increasing trend, rising from 1.35 T to 1.84 T under peak operating conditions. Taking into account the machine's temperature rise under the S2 duty cycle and its hill-climbing capability under maximum load, the suitable range for the stator slot width is determined to be between 4.5 mm to 4.85 mm, a value of 4.7 was selected for the calculation.

4. Optimization of Machine Design

4.1. Optimization Strategy

Based on the aforementioned studies, which completed the design of the machine's electric and magnetic loadings and determined the fundamental dimensions of the stator teeth and slots, this section will focus on optimizing the machine's output performance. Due to the complex duty cycle of golf cart operations, the optimization will use rotor parameters as design variables to meet vehicle requirements for drive system torque, torque ripple, efficiency, and other criteria. The optimization process is divided into two stages. The first stage involves a no-load optimization, focusing on the flux linkage and cogging torque under no-load conditions. The second stage addresses optimization under rated load conditions, with emphasis on the machine's rated output torque, torque ripple magnitude, and operational efficiency. The optimization was performed using a coupled simulation approach integrating ANSYS Electronics Desktop 2021R1 for electromagnetic finite element analysis and ANSYS Workbench 2021R1 for implementing the optimization algorithm. The MOGA implemented in this study is based on the Non-dominated Sorting Genetic Algorithm II framework. For both optimization stages, the algorithm was configured with a population size of 50 and was run for 20 generations, which served as the stopping criterion. The constraints defined in Equations (5) and (6) were enforced using a static penalty function method, which penalizes infeasible solutions by severely worsening their objective function value, thereby effectively guiding the search towards the feasible region

of the design space. The machine's parameter variables are illustrated in Figure 6, and the division of the optimization stages is summarized in Table 4. The flow chart of the optimization design is shown in Figure 7.

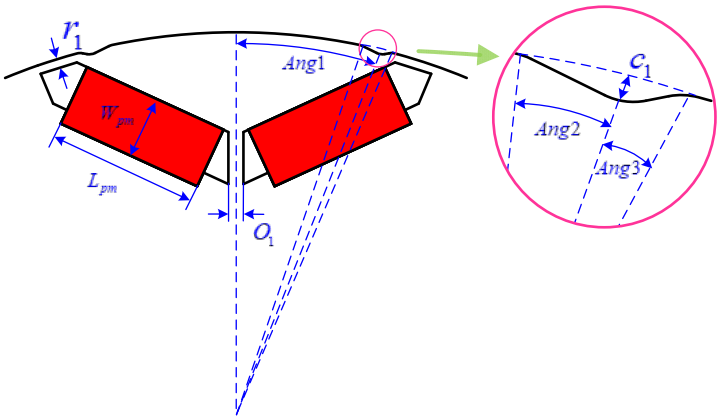


Figure 6. Design variables for machine optimization.

Table 4. Optimization stages, objectives, and variables.

Stages	Objectives	Variables
I: No-load optimization	Fluxlinkage (ψ_d) Cogging torque (T_{cog})	L_{pm}: 9.5–12.5 mm W_{pm}: 4.0–6.0 mm O_1: 0.8–1.6 mm r_1: 0.8–1.4 mm
II: Rated load optimization	Torque (T_{out}) Torque ripple (T_{ripple}) Efficiency (η_m)	O_1: based on stage 1 results r_1: based on stage 1 results Ang_1: 10–22° Ang_2: 0.5–3.5° Ang_3: 0.5–3.5° c_1: 0.1–0.5 mm

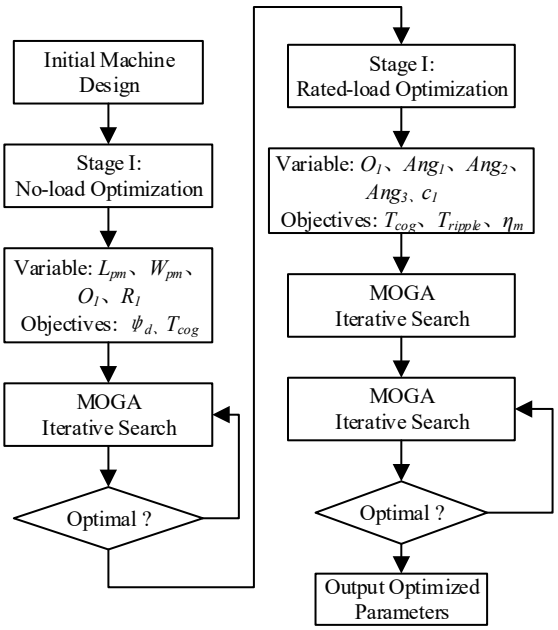


Figure 7. Flowchart of the two-stage optimization strategy.

The variation ranges for the design variables listed in Table 4 were determined based on a combination of prior electromagnetic sensitivity studies and practical mechanical

constraints, such as ensuring rotor structural integrity and maintaining manufacturable feature sizes.

4.2. Objective Functions and Constraints

The machine designed in this project operates from a 48 V DC battery supply, which is classified as a low-voltage system. To fulfill the vehicle's need for frequent hill climbing, the electromagnetic design must support low-voltage, high-current operation. A lower supply voltage inherently leads to a lower back-EMF, implying that the no-load flux linkage should not be set too high. Nevertheless, an excessively low flux linkage negatively impacts torque output performance. Thus, it is essential to maintain the no-load flux linkage within an appropriate range.

Additionally, cogging torque, a periodic torque ripple inherent to permanent magnet machines resulting from the interaction between stator slots and permanent magnets, can cause speed fluctuations and hinder smooth operation at low speeds if excessive. Consequently, the objectives and constraints for the no-load optimization stage are defined as follows:

$$\begin{cases} \text{Function}: [Max\ f(\psi_d),\ Min\ f(T_{cog})] \\ \text{Constraints}:\ 0.018\text{Wb} \le \psi_d \le 0.020\text{Wb},\ T_{cog} \le 0.15\text{Nm} \end{cases} \tag{5}$$

The bounds for the no-load optimization were defined based on fundamental system constraints. The flux linkage range of 0.018–0.020 Wb was determined by a trade-off between the torque requirement for hill climbing and the safety limit imposed by the 48 V DC bus voltage, ensuring the back EMF remains within a safe range at the maximum speed. The cogging torque limit of 0.15 Nm (<1% of rated torque) was set to meet the NVH requirements for smooth low-speed operation, which is critical for passenger comfort in golf carts.

The frequent operating conditions of the vehicle correspond to the machine's rated state. To achieve higher efficiency, greater output torque, and smoother output during these frequent operating conditions, the second-stage optimization for rated conditions defines the machine's output torque (T_{out}), torque ripple (T_{ripple}), and rated efficiency (η_m) as optimization objectives, based on the multi-condition operational requirements of golf carts. The optimization objectives and constraints are as follows:

$$\begin{cases} \text{Function}: [Max\ f(T_{out}),\ Min\ f(T_{ripple}),\ Max\ f(\eta_m)] \\ \text{Constraints}:\ T_{out} \ge 18.8\text{Nm}, T_{ripple} \le 1.7\text{Nm},\ \eta_m \ge 95\% \end{cases} \tag{6}$$

The targets for the rated-load optimization were derived from application-specific requirements. The torque target (≥18 Nm) incorporates a safety margin over the calculated requirement to account for manufacturing tolerances. The torque ripple limit (≤1.7 Nm, <10% of rated torque) is an industry benchmark for smooth operation, directly linked to vehicle NVH performance. The efficiency target (≥95%) is essential for maximizing battery life and range, aligning with the core objective of developing an eco-friendly drive system.

Once the optimization objectives and constraints are defined, the optimization model for minimizing $f(x_i)$ can be expressed as follows [21,22]:

$$f(x_i) = \lambda_1 \frac{T_{\text{out}}{}'}{T_{out}(x_i)} + \lambda_2 \frac{T_{ripple}(x_i)}{T_{ripple}{}'} + \lambda_3 \frac{\eta_m(x_i)}{\eta_m{}'} \tag{7}$$

In the equation, $T_{out}{}'$, $T_{ripple}{}'$, and $\eta_m{}'$ represent the initial values of the rated output torque, torque ripple, and rated efficiency, respectively. The parameters λ_1, λ_2, and λ_3

denote the weighting coefficients for the output torque, torque ripple, and efficiency, respectively. A higher weighting coefficient indicates a greater priority for the corresponding objective, with the constraint that $\lambda_1 + \lambda_2 + \lambda_3 = 1$.

4.3. No-Load Condition Optimization

Under no-load conditions, the magnetic field is exclusively generated by permanent magnets, with all flux in both stator and rotor originating from these magnets. During this optimization stage, the permanent magnet thickness (W_{pm}) and length (L_{pm}) determine the magnitude of the flux linkage produced. Meanwhile, the center magnetic bridge (O_1) and end magnetic bridge (r_1) of the permanent magnets govern the amount of flux that effectively reaches the stator side. This is because substantial flux leakage occurs through bridges O_1 and r_1; wider bridges result in increased leakage flux, consequently reducing the useful flux crossing the air gap and entering the stator.

Figure 8 presents the response surfaces illustrating the influence of permanent magnet dimensions on the no-load flux linkage, along with the effects of the end and center bridge lengths. As corroborated by the preceding analysis, the L_{pm} and W_{pm} demonstrate a decisive impact on flux linkage, with increased magnet length proving particularly advantageous for enhancing flux linkage. The r_1 and O_1 primarily mediate their influence through flux leakage effects, thereby indirectly affecting the flux linkage in the stator.

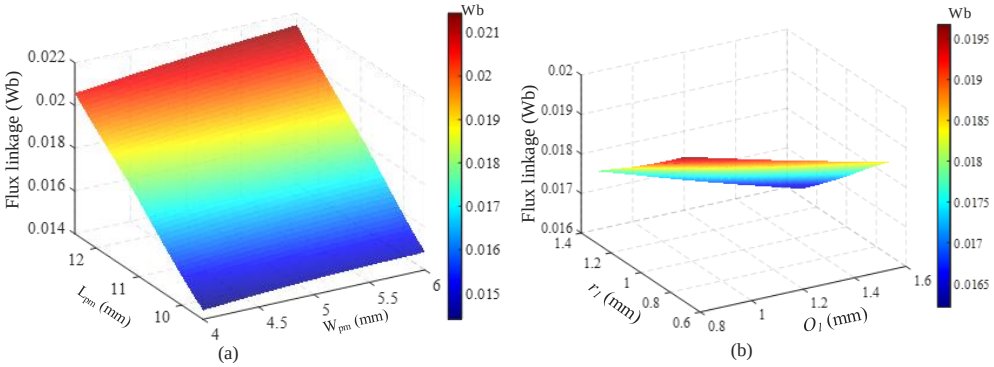


Figure 8. Effect of optimization variables in stage I on flux linkage. (**a**) Effect of L_{pm} and W_{pm} on flux linkage. (**b**) Effect of r_1 and O_1 on flux linkage.

Figure 9 presents the response surfaces illustrating the influence of the four parameters on cogging torque. As shown in Figure 9a, W_{pm} exhibits a linear and relatively minor effect on cogging torque, while the L_{pm} demonstrates a more substantial influence. As L_{pm} increases, the cogging torque initially rises then decreases, reaching its peak at approximately L_{pm} = 11.5 mm. Therefore, the selection of L_{pm} should extend beyond this peak point. Figure 9b reveals that larger end magnetic bridge (r_1) values combined with smaller center magnetic bridge (O_1) values result in increased cogging torque. Consequently, while ensuring rotor structural integrity, minimizing r_1 and maximizing O_1 values is recommended.

Based on the optimization objectives and constraints defined for the no-load stage, a MOGA was employed to optimize the four variables. Figure 10 illustrates the trade-off between the no-load flux linkage and no-load cogging torque. The feasible region satisfying the constraints in Equation (3) is represented by the pink-shaded area in the figure. Integrating these results with the machine magnetic flux density requirements established previously, the permanent magnet dimensions were ultimately determined as 12.2 mm in length and 4.8 mm in width.

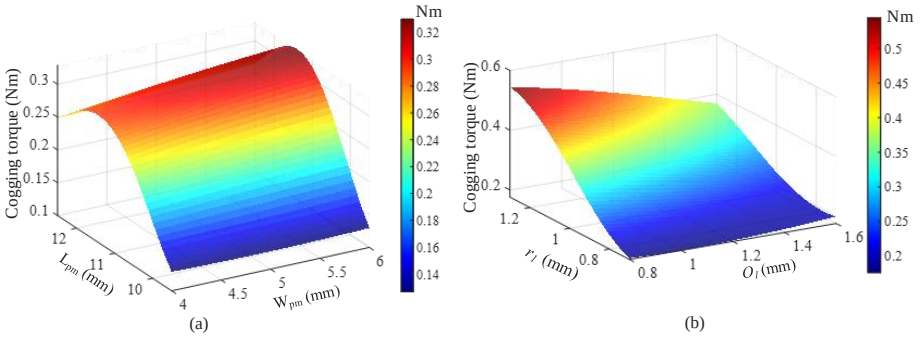


Figure 9. Effect of optimization variables in stage I on cogging torque. (**a**) Effect of L_{pm} and W_{pm} on cogging torque. (**b**) Effect of r_1 and O_1 on cogging torque.

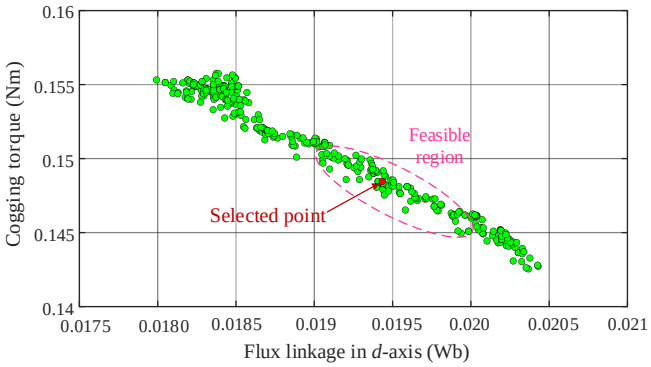


Figure 10. The trade-off between the no-load flux linkage and no-load cogging torque.

4.4. Rated Load Condition Optimization

During the rated load optimization stage, six variables and three optimization objectives were established. The design variables exhibit varying degrees of influence on each optimization objective. To effectively identify the impact of each design variable on the targets, this study employs sensitivity analysis to investigate the relationships between individual variables and optimization objectives. Here, the sensitivity index $H(x_i)$ can be expressed as [23]:

$$H(x_i) = \frac{V(E(y/x_i))}{V(y)} \tag{8}$$

where x_i represents the design variable, y denotes the optimization objective, $E(y \mid x_i)$ is the mean value of the optimization objective y when variable x_i remains constant, and $V(E(y \mid x_i))$ and $V(y)$ represent the variances of $E(y \mid x_i)$ and y, respectively.

The results of the sensitivity analysis are presented in Figure 11. Generally, the magnitude of the sensitivity index value indicates the degree of influence a variable has on the objective. A positive sensitivity index indicates that the metric increases with the design variable, while a negative sensitivity index demonstrates the opposite trend.

Regarding output torque, variables r_1 and O_1 exhibit significant influence with negative sensitivity coefficients, indicating that to ensure higher torque output, the end magnetic bridge (r_1) and center magnetic bridge (O_1) of the permanent magnets should not be excessively large. For torque ripple, with the exception of magnetic bridge O_1 which demonstrates negligible impact, the other five parameters substantially affect its magnitude. To reduce torque ripple, consideration should be given to increasing parameters ang_1, c_1, and r_1 while decreasing parameters ang_2 and ang_3. As for efficiency, parameter c_1 shows a positive yet relatively small sensitivity coefficient, while all other parameters demonstrate negative sensitivity coefficients. This suggests that except for parameter c_1, reducing the values of the other parameters is beneficial for improving efficiency. It is evident that

the influences of various parameters on the optimization objectives are interwoven and relatively complex, necessitating further trade-off design between the competing objectives.

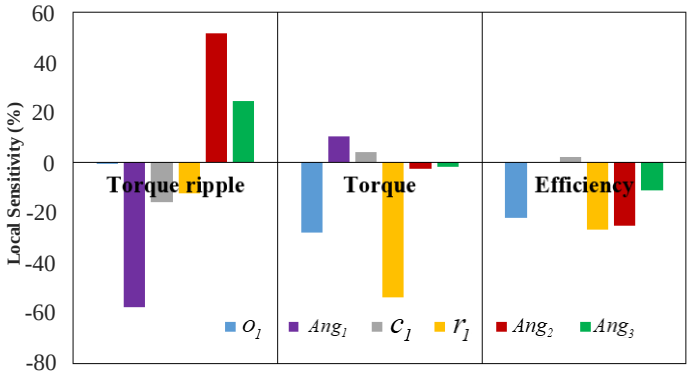


Figure 11. Parameter sensitivity analysis for stage II optimization objectives.

In this stage, the MOGA was again employed for optimization. Based on the constraints specified in Equation (6), the minimum value of $f(x_i)$ in Equation (7) was determined. The obtained $f(x_i)_{\min}$ represents the comprehensive optimal solution for the three optimization variables, with the corresponding parameters constituting the optimal design parameters for the machine.

Figure 12 illustrates the trade-off relationships among torque, torque ripple, and efficiency. The point marked with a red pentagram indicates the optimal solution that balances all three optimization objectives. The output torque, torque ripple, and efficiency corresponding to this point represent the machine performance achieved under this optimal solution. The optimal values for the six design variables corresponding to the selected candidate point are as follows: O_1 = 1.2 mm, r_1 = 0.8 mm, Ang_1 = 15°, Ang_2 = 1.2°, Ang_3 = 1.9°, and c_1 = 0.35 mm.

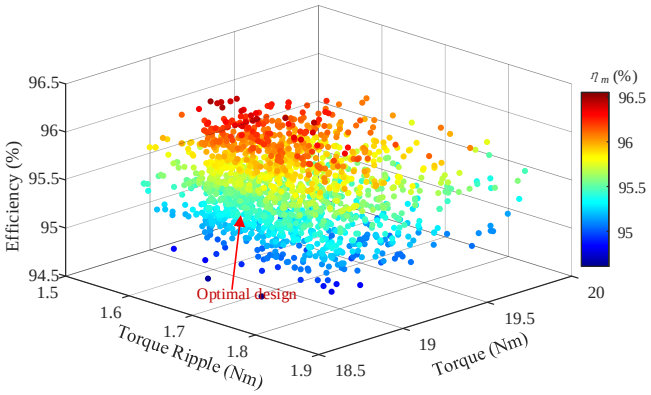


Figure 12. The optimization results of the three optimization objectives in stage II.

5. Performance Analysis

5.1. No-Load Operation Performance Analysis

Under no-load conditions, the key parameters of interest are the no-load back EMF and the cogging torque. Performance of the machine under no-load operation was simulated using ANSYS Electronics Desktop 2021R1. Figure 13 shows the cogging torque curves of the machine over one electrical cycle. It can be observed that the cogging torque is significantly reduced after optimization, decreasing from ±328 mNm to ±126 mNm. This reduction contributes to improved starting characteristics and enhances operational smoothness of the machine at low speeds.

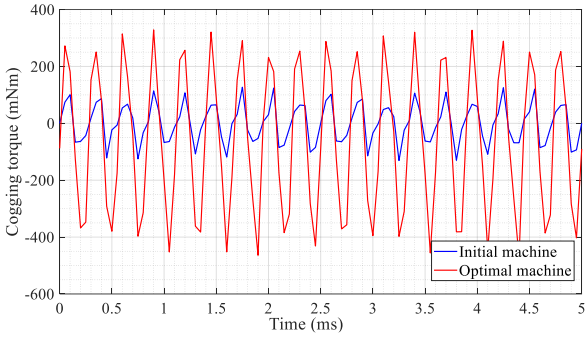


Figure 13. Comparison of no-load cogging torque before and after optimization.

Figure 14 compares the back EMF under no-load conditions before and after optimization. It can be observed that at a speed of 3000 rpm, the optimized machine exhibits a lower back EMF amplitude compared to the initial design, which is attributed to the reduced usage of permanent magnets in the optimized model. However, the sinusoidal quality of the back EMF waveform is noticeably improved after optimization. This is quantitatively confirmed by the total harmonic distortion (THD), which is reduced from 9.68% in the initial design to 7.52% in the optimized one. Furthermore, Fourier analysis of the back EMF reveals that the fundamental component is slightly lower in the optimized design. More importantly, the amplitudes of the predominant harmonics are reduced to a greater extent, leading to an improved sinusoidal waveform and the observed reduction in total harmonic distortion.

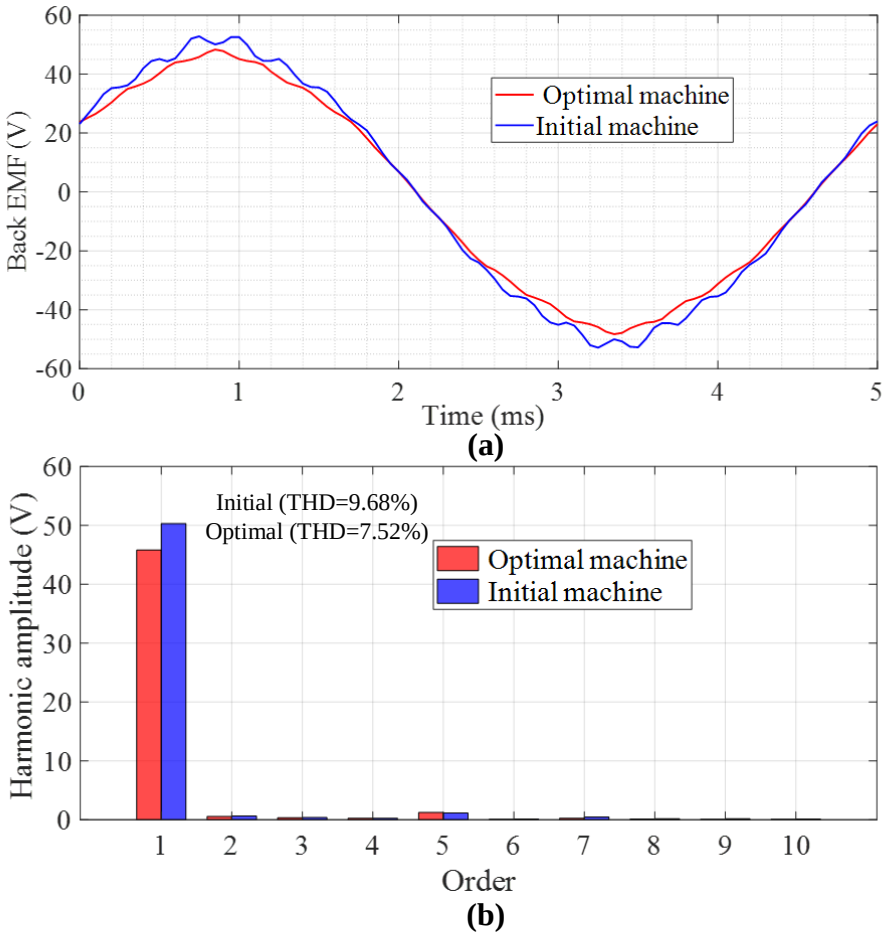


Figure 14. Comparison of No-Load Back EMF before and after optimization. (**a**) Back EMF Waveform. (**b**) Fourier Analysis of the Back EMF.

5.2. Rated-Load Operation Performance Analysis

The rated operating condition represents the most frequent working state for the golf cart; therefore, particular attention must be paid to the machine's torque and efficiency under this regime. It should be noted that the machine efficiency presented in this section is calculated based on electromagnetic losses. Specifically, it considers the measured stator copper losses and the core losses derived from finite-element analysis, while mechanical losses such as bearing friction and windage are excluded from this calculation. First, a comparative analysis of the output torque before and after optimization was conducted. Figure 15 shows the total output torque and reluctance torque of the machine at different current angles. It can be observed that after optimization, the maximum torque increases from 17.9 Nm to 19.2 Nm. The optimized machine not only delivers higher torque but also exhibits a greater reluctance torque component. This enhancement is primarily attributed to the increased saliency ratio, which rose from 2.03 to 2.24 after optimization, thereby strengthening the reluctance torque path. This indicates that for the same torque output, the optimized design requires less permanent magnet material, as quantified by a 4.75% reduction in magnet mass, which is beneficial for reducing overall machine cost.

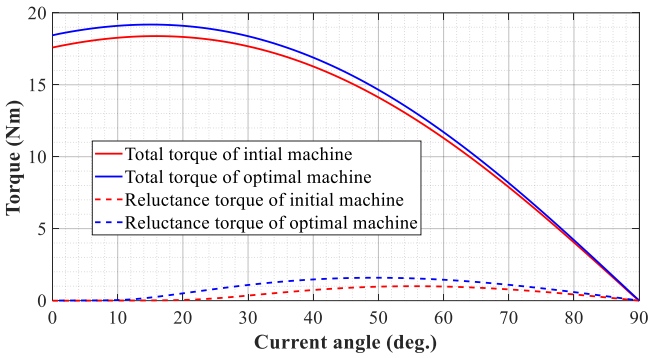


Figure 15. Torque comparison at different current Angles before and after optimization.

Figure 16 presents a comparison of torque ripple before and after machine optimization. It can be observed that over one electrical cycle under identical operating conditions with a rated current of 92 A and a rated speed of 3000 rpm, the optimized machine not only delivers higher output torque but also exhibits significantly reduced torque fluctuation. The peak-to-peak torque value decreases from 2.1 Nm in the initial design to 1.6 Nm after optimization. This improvement is instrumental in enhancing vehicle ride comfort, suppressing noise, and ultimately improving the overall NVH performance.

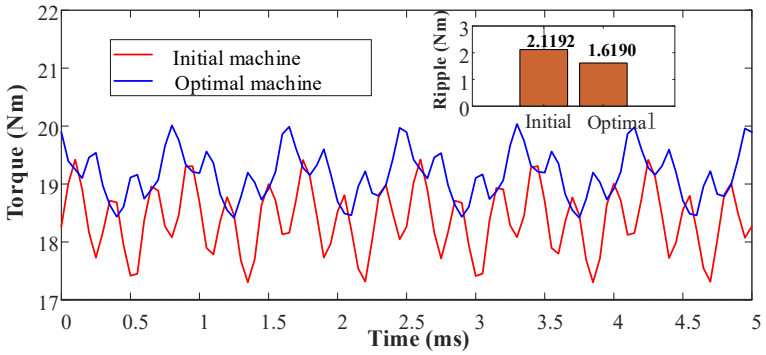


Figure 16. Comparison of torque ripple before and after machine optimization.

When mechanical losses and additional losses are neglected, the machine's efficiency is determined solely by the core losses in the stator and rotor and the copper losses in

the windings. To investigate the efficiency performance of the optimized machine, the loss characteristics and efficiency before and after optimization were analyzed. Figure 17a illustrates the core loss and efficiency under different current amplitudes and current angles for both the initial and optimized designs. Since the number of winding turns and the winding configuration remain unchanged after optimization, the copper losses under the same input current are identical for both designs. Therefore, the analysis focuses specifically on the variation in core losses.

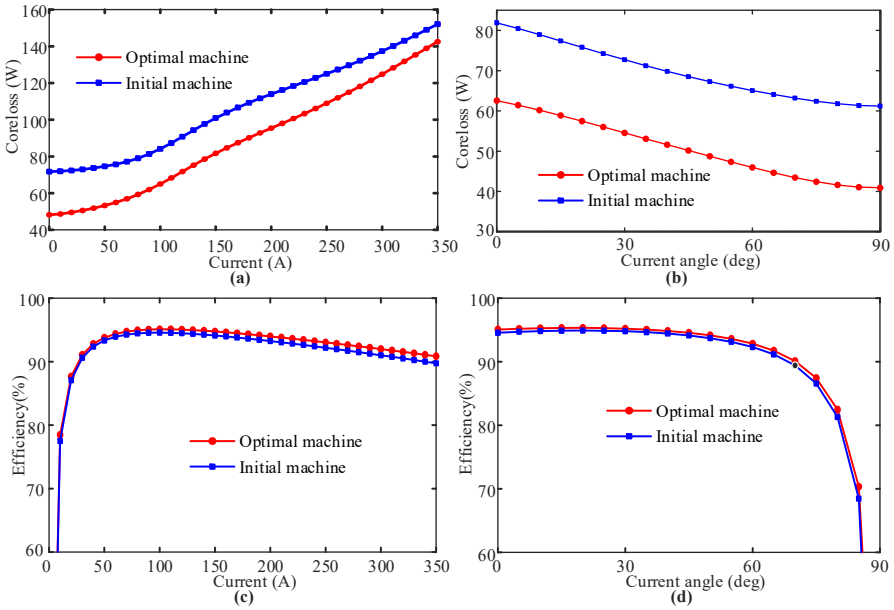


Figure 17. The core loss and efficiency under different current amplitudes and current angles for both the initial and optimized designs. (**a**) Core loss vs. current. (**b**) Core loss vs. current angle. (**c**) Efficiency vs. current. (**d**) Efficiency vs. current angle.

As shown in Figure 17b, the core loss increases with the input current, and the optimized machine exhibits lower core losses compared to the original design. Furthermore, within the current angle range of 0 to 90 degrees, the optimized machine consistently demonstrates reduced core losses, indicating lower high-speed losses during flux-weakening operation. From Figure 17c, it can be observed that as the current increases, the efficiency difference between the initial and optimized designs becomes more pronounced. At 350 A, the optimized machine achieves an efficiency improvement of 1.2%, demonstrating its ability to deliver higher efficiency during heavy-load operations such as vehicle hill climbing. Figure 17d further confirms that the optimized machine maintains its efficiency advantage under flux-weakening conditions as well.

6. Experimental Verification

In order to further verify the feasibility of the machine topology and the effectiveness of the proposed optimal method, an experimental prototype is fabricated. It should be noted that the simulated efficiency maps are derived from electromagnetic losses (core and copper losses) only, whereas the measured results inherently include additional mechanical losses such as bearing friction and windage. The test was conducted on a dynamometer system. A programmable DC power supply provided the 48 V input, while torque, speed, and electrical parameters were measured with a torque transducer and a precision power analyzer. The test platform, along with the stator and rotor of the electric machine, is shown in Figure 18.

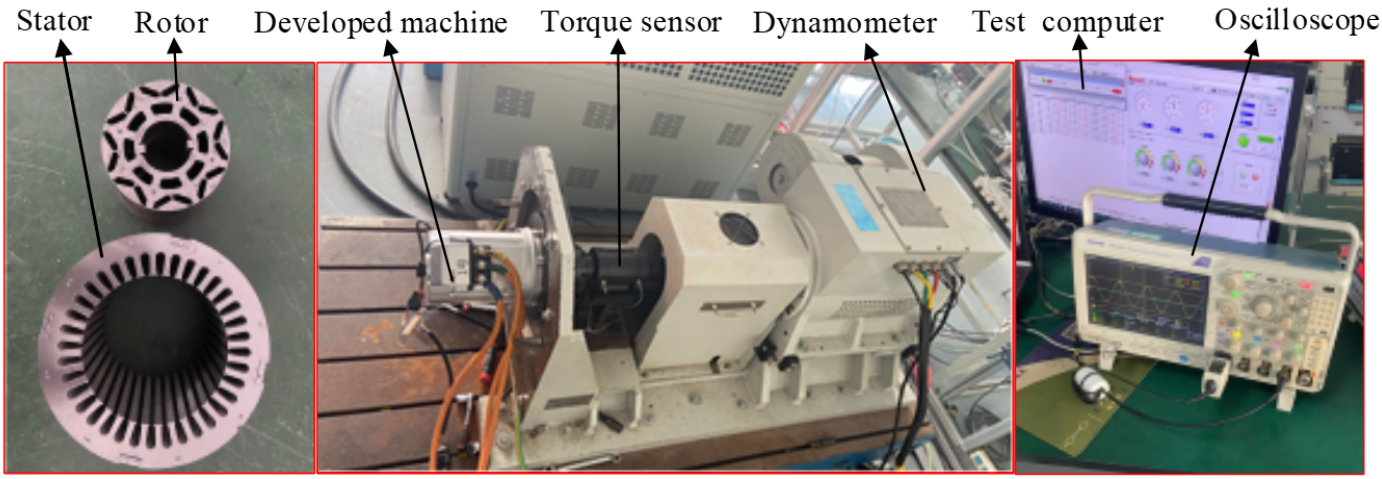


Figure 18. View of the test platform and machine components.

The no-load back EMF of the prototype machine was measured at the maximum speed of 7200 rpm to validate its no-load characteristics, as shown in Figure 19. Figure 19a,b display the back EMF waveforms obtained from testing and simulation, respectively. A close examination reveals a strong agreement between the two waveforms. The measured back EMF at the maximum speed is approximately 101 V, which deviates by only 2.96% from the simulated value of 98.1 V. This close consistency verifies the rationality of the machine design.

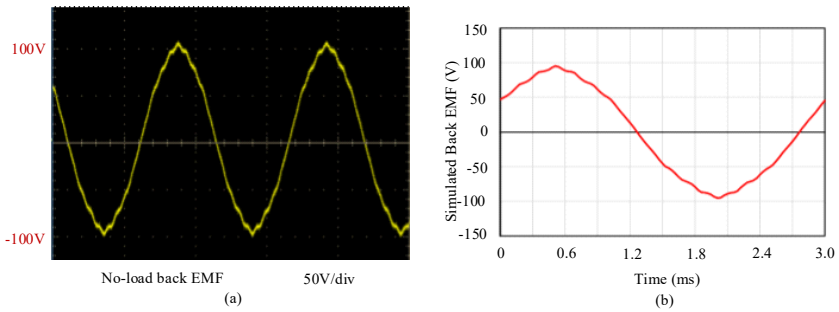


Figure 19. The waveform of back EMF at maximum motor speed. (**a**) Measured back EMF. (**b**) Simulated back EMF.

A comparison between the measured and simulated torque of the machine is provided in Figure 20. As shown, both the measured and simulated torque values increase with rising machine current, exhibiting a consistent growth trend. Owing to the stacking factor of the laminations in the actual prototype and manufacturing tolerances, the simulated torque is slightly higher than the measured torque. At a machine current of 390 A, the measured torque value is 75.2 Nm, which satisfies the torque requirement for the maximum slope-climbing condition of the golf cart.

Figure 21 presents the simulated efficiency map of the machine alongside an efficiency map generated from test data. As observed, the efficiency distribution patterns between simulation and test results are generally consistent. Both maps indicate lower efficiency in the low-speed high-torque and high-speed regions, while the high-efficiency area is concentrated within the 2000 to 4000 rpm range. A peak efficiency of 95% is achieved in both cases, which validates the rationality of the machine structure and its optimization design. The minor reduction in the measured peak efficiency, compared to the simulation, is primarily attributed to unmodeled mechanical losses inherent in the physical prototype, as the simulation accounts for electromagnetic losses only.

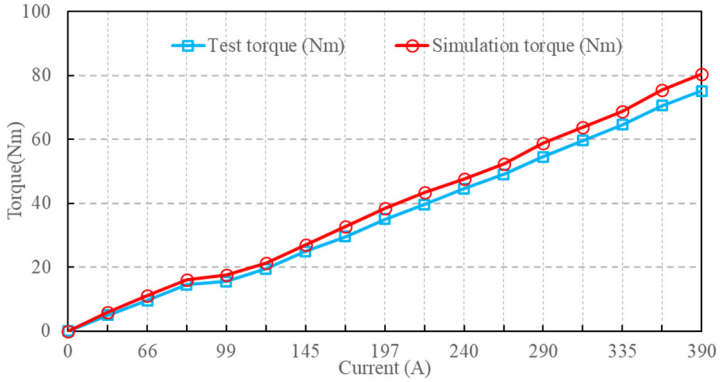


Figure 20. Comparison between the measured and simulated torque of the machine.

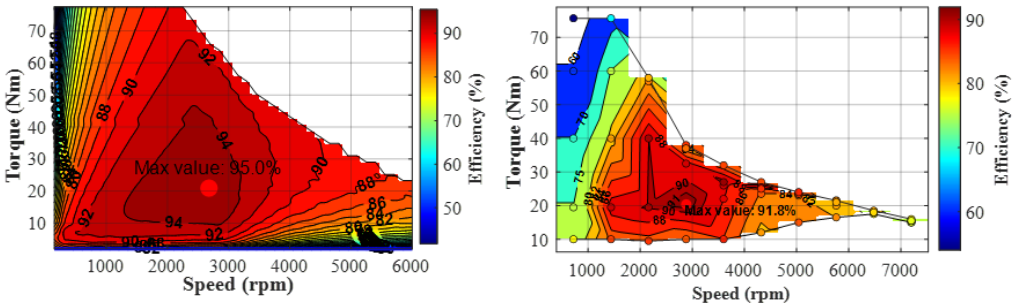


Figure 21. Measured and simulated machine efficiency maps.

7. Conclusions

This paper successfully designed and optimized a 36-slot 8-pole interior PMSM for golf carts using a two-stage multi-objective method. The optimization balanced key performance metrics under multiple operating conditions. The final design demonstrates significant improvements: cogging torque was reduced by over 60%, rated output torque increased to 19.2 Nm, torque ripple was minimized, and operational efficiency was enhanced. Experimental results closely match simulations, validating the effectiveness of the proposed method. The optimized machine meets the demanding requirements of golf cart applications, offering high performance, smooth operation, and improved energy efficiency across diverse driving scenarios. The systematic two-stage optimization strategy, coupled with the MOGA, proves highly effective in decoupling conflicting design objectives and achieving a well-balanced performance enhancement across both no-load and rated-load conditions. Furthermore, the optimized design achieves these performance gains while reducing the usage of expensive permanent magnet material by 4.75%, highlighting its practical value for cost-sensitive applications. Future work will focus on investigating the thermal management under prolonged high-load operations, such as continuous hill climbing, to further ensure the machine's reliability and durability.

Author Contributions: Conceptualization, W.W. (Wenye Wu); methodology, W.W. (Wenye Wu) and D.L.; software, W.W. (Wenye Wu) and W.W. (Weifeng Wang); validation, W.W. (Wenye Wu), D.L. and W.W. (Weifeng Wang); formal analysis, W.W. (Wenye Wu); investigation, W.W. (Wenye Wu), D.L. and W.W. (Weifeng Wang); resources, W.W. (Wenye Wu); data curation, W.W. (Wenye Wu); writing—original draft preparation, W.W. (Wenye Wu); writing—review and editing, W.W. (Wenye Wu); visualization, W.W. (Wenye Wu); supervision, W.W. (Wenye Wu); project administration, W.W. (Wenye Wu); funding acquisition, W.W. (Wenye Wu). All authors have read and agreed to the published version of the manuscript.

Funding: This research was funded by the Ministry of Education Industry—University Collaborative Education Program, grant number 231000805254336.

Data Availability Statement: The original contributions presented in the study are included in the article; further inquiries can be directed to the corresponding author.

Acknowledgments: The authors wish to express their gratitude to Wuxi Huasheng Litong Electric Drive System Co., Ltd. for their assistance in the fabrication of the machine prototype.

Conflicts of Interest: Author Weifeng Wang was employed by the company NBSL M&E TECHNOLOGY Co., Ltd. The remaining authors declare that the research was conducted in the absence of any commercial or financial relationships that could be construed as a potential conflict of interest.

Abbreviations

T_{tq}	Vehicle drive machine torque (Nm)
i	Vehicle drive ratio
η_T	Vehicle transmission efficiency (%)
r	Wheel radius (m)
m	Vehicle mass (kg)
g	Gravitational force (m/s^2)
f	Rolling resistance coefficient
α	Slope angle (°)
ρ	Air density ($\approx$1.225 kg/m^3)
C_d	Air resistance coefficient
A	Frontal area of the vehicle (m^2)
u_a	Vehicle speed (km/h)
δ	Vehicle rotational mass conversion coefficient
du/dt	Vehicle acceleration (m/s^2)
P_e	Drive machine power (kW)
w_s	Stator slot width (mm)
w_t	Stator tooth width (mm)
k_s	Saturation coefficients of the stator/rotor iron cores
k_δ	Saturation coefficients of air gap
δ_g	Air gap length (mm)
μ_0	Relative permeability of the iron core
B_δ	Magnetic flux density in the air gap (T)
B_r	The remanent magnetic density of permanent magnet (T)
H_c	The coercivity of permanent magnet (A/m)
J_1, J_2	Rated current density, Peak current density (A/mm^2)
B_1, B_2, B_3	No-load flux density, Rated flux density, Peak flux density (T)
L_{pm}	Permanent magnet thickness (mm)
W_{pm}	Permanent magnet length (mm)
O_1	Center magnetic bridge of the permanent magnets (mm)
r_1	End magnetic bridge of the permanent magnets (mm)
Ang_1	Angle between auxiliary slot bottom and the centerline (mm)
Ang_2	Angle between auxiliary slot bottom and left-side vertex (mm)
Ang_3	Angle between auxiliary slot bottom and right-side vertex (mm)
c_1	Auxiliary slot depth (mm)
ψd	Fluxlinkage in d-axis (Wb)
$Tcog$	Cogging torque (Nm)
T_{out}	Output torque (Nm)
T_{ripple}	Torque ripple (Nm)
η_m	Machine efficiency (%)

References

1. Martín-García, M.d.; Ruiz-Real, J.L.; Gazquez-Abad, J.C.; Uribe-Toril, J. Why Do We Play Golf? An Exploratory Research. In *Disruptions, Diversity, and Ethics in Marketing, Proceedings of the International Conference on Advanced Marketing Practice, Almeria, Spain, 18–19 April 2024*; Springer: Cham, Switzerland, 2025.
2. Tassiopoulos, D.; Haydam, N. Golf Tourists in South Africa: A Demand-Side Study of a Niche Market in Sports Tourism. *Tour. Manag.* **2008**, *29*, 870–882. [CrossRef]
3. Molina, M.A.; Del Campo, F.J.; López, D.B.; Agulló, A.M. Analysis of the opinion about economic and social impacts of golf courses in a tourist destination. *World J. Entrep. Manag. Sustain. Dev.* **2010**, *6*, 103–117.
4. Timilsina, R.R.; Zhang, J.; Rahut, D.B.; Patradool, K.; Sonobe, T. Global drive toward net-zero emissions and sustainability via electric vehicles: An integrative critical review. *Energy Ecol. Environ.* **2025**, *10*, 125–144. [CrossRef]
5. Trivedi, V.; Saxena, A.; Javed, M.; Kumar, P.; Singh, V. Design of Six Seater Electrical Vehicle (Golf Cart). *Evergr. J. Nov. Carbon Resour. Sci. Green Asia Strategy* **2023**, *10*, 953–961. [CrossRef]
6. Ozer, K.; Yilmaz, M. Design and Optimization of IPMSM for Enhanced Efficiency, Cost Reduction, and Performance in Light Electric Vehicles. *IEEE Access* **2025**, *13*, 80621–80635. [CrossRef]
7. Storey, J.M.E.; Lewis, S.A., Sr. *Golf Cars: Emissions, Noise, and Performance Characteristics*; Oak Ridge National Laboratory: Oak Ridge, TN, USA, 2008.
8. Emadi, A. (Ed.) *Handbook of Automotive Power Electronics and Motor Drives*; CRC Press: Boca Raton, FL, USA, 2017.
9. Liu, H.D.; Hung, Y.H.; Lin, J.T.; Huang, L.C.; Shih, J.W.; Li, C. Development of an Intelligent Transportation-Oriented Autonomous Driving Assistance System and Energy Efficiency Optimization Based on Electric Golf Cart Battery Packs. *Energy* **2025**, *335*, 138116. [CrossRef]
10. Ran, Z.; Zhu, Z.Q.; Chen, Z.; Younkins, M.; Farah, P. Novel System-Level Driving-Cycle-Oriented Design Co-Optimization of Electrical Machines for Electrical Vehicles. *IEEE Access* **2024**, *12*, 106530–106545. [CrossRef]
11. Yamazaki, K.; Kumagai, M. Torque Analysis of Interior Permanent-Magnet Synchronous Motors by Considering Cross-Magnetization: Variation in Torque Components with Permanent-Magnet Configurations. *IEEE Trans. Ind. Electron.* **2014**, *61*, 3192–3201. [CrossRef]
12. Huang, C.; Li, H.; Li, S.; Sun, Y. Multi-Objective Optimization Design of Low-Torque Ripple Ferrite-Assisted Synchronous Reluctance Motor. *Prog. Electromagn. Res. C* **2024**, *146*, 119–130. [CrossRef]
13. Wang, Y.; Zhao, M.; Jia, X.; Lu, M. Analysis and Multi-Objective Optimization of an Interior Permanent Magnet Synchronous Motor for a Comprehensive Performance Enhancement. *Struct. Multidiscip. Optim.* **2025**, *68*, 55. [CrossRef]
14. Ma, S.; Chen, K.; Zhang, Q. Analysis of Multi-Objective Optimization Design of Interior Double Radial and Tangential Combined Magnetic Pole Permanent Magnet Drive Motor for Electric Vehicles. *World Electr. Veh. J.* **2024**, *15*, 142. [CrossRef]
15. Zhu, Z.Q.; Howe, D. Influence of design parameters on cogging torque in permanent magnet machines. *IEEE Trans. Energy Convers.* **2002**, *15*, 407–412. [CrossRef]
16. Bianchi, N.; Bolognani, S. Design techniques for reducing the cogging torque in surface-mounted PM motors. *IEEE Trans. Ind. Appl.* **2002**, *38*, 1259–1265. [CrossRef]
17. You, Y.M. Multi-Objective Optimal Design of Permanent Magnet Synchronous Motor for Electric Vehicle Based on Deep Learning. *Appl. Sci.* **2020**, *10*, 482. [CrossRef]
18. Zhang, H.; Wang, G.; Zhang, J.; Gao, Y.; Hua, W.; Wang, Y. An Improved Kriging Surrogate Model Method with High Robustness for Electrical Machine Optimization. *IEEE Trans. Ind. Appl.* **2024**, *60*, 6799–6809. [CrossRef]
19. Pagare, A.; Shewalkar, S.; Yadav, S.; Dhake, D. Simulation and Analysis of Solar-Powered Electric Golf Cart. In Proceedings of the 2024 4th Asian Conference on Innovation in Technology (ASIANCON), Pimari Chinchwad, India, 23–25 August 2024; pp. 1–8.
20. Gillespie, T. (Ed.) *Fundamentals of Vehicle Dynamics*; SAE International: Warrendale, PA, USA, 2021.
21. Wang, Y.; Niu, S.; Fu, W.N. Design and Optimization of Electric Continuous Variable Transmission System for Wind Power Generation. *IEEE Trans. Magn.* **2016**, *52*, 8200704. [CrossRef]
22. Wang, J.; Yuan, X.; Atallah, K. Design Optimization of a Surface-Mounted Permanent-Magnet Motor with Concentrated Windings for Electric Vehicle Applications. *IEEE Trans. Veh. Technol.* **2013**, *62*, 1053–1064. [CrossRef]
23. Saltelli, A.; Annoni, P.; Azzini, I.; Campolongo, F.; Tarantola, S. Variance based sensitivity analysis of model output design and estimator for the total sensitivity index. *Comput. Phys. Commun.* **2010**, *181*, 259–270. [CrossRef]

Disclaimer/Publisher's Note: The statements, opinions and data contained in all publications are solely those of the individual author(s) and contributor(s) and not of MDPI and/or the editor(s). MDPI and/or the editor(s) disclaim responsibility for any injury to people or property resulting from any ideas, methods, instructions or products referred to in the content.